

# Accepted Manuscript

Rational design of integrated  $\text{CuO@Co}_x\text{Ni}_{1-x}(\text{OH})_2$  nanowire arrays on copper foam for high-rate and long-life supercapacitors

Shuxing Wu, Hengzhi Guo, Kwan San Hui, Kwun Nam Hui



PII: S0013-4686(18)32445-9

DOI: <https://doi.org/10.1016/j.electacta.2018.10.183>

Reference: EA 32982

To appear in: *Electrochimica Acta*

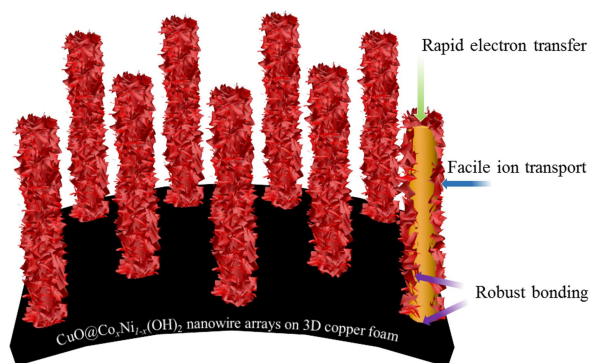
Received Date: 19 July 2018

Revised Date: 5 October 2018

Accepted Date: 30 October 2018

Please cite this article as: S. Wu, H. Guo, K.S. Hui, K.N. Hui, Rational design of integrated  $\text{CuO@Co}_x\text{Ni}_{1-x}(\text{OH})_2$  nanowire arrays on copper foam for high-rate and long-life supercapacitors, *Electrochimica Acta* (2018), doi: <https://doi.org/10.1016/j.electacta.2018.10.183>.

This is a PDF file of an unedited manuscript that has been accepted for publication. As a service to our customers we are providing this early version of the manuscript. The manuscript will undergo copyediting, typesetting, and review of the resulting proof before it is published in its final form. Please note that during the production process errors may be discovered which could affect the content, and all legal disclaimers that apply to the journal pertain.



## Rational Design of Integrated $\text{CuO@Co}_x\text{Ni}_{1-x}(\text{OH})_2$ Nanowire Arrays on Copper Foam for High-Rate and Long-Life Supercapacitors

Shuxing Wu <sup>a,†</sup>, Hengzhi Guo <sup>b,†</sup>, Kwan San Hui <sup>c,\*</sup>, Kwun Nam Hui <sup>d,\*\*</sup>

<sup>a</sup> School of Chemical Engineering and Light Industry, Guangdong University of Technology, Guangzhou 510006, PR China

<sup>b</sup> Department of Mechanical Convergence Engineering, Hanyang University, 17 Haengdang-dong, Seongdong-gu, Seoul 133-791, Republic of Korea

<sup>c</sup> Faculty of Science and Engineering, University of East Anglia, Norwich, NR4 7TJ, United Kingdom

<sup>d</sup> Institute of Applied Physics and Materials Engineering, University of Macau, Avenida da Universidade, Macau, China

<sup>†</sup> Shuxing Wu and Hengzhi Guo contributed equally to this work

\*Corresponding author:

E-mail: k.hui@uea.ac.uk (Kwan San Hui)

E-mail: bizhui@umac.mo (Kwun Nam Hui)

**Abstract**

Rational electrode architectural design, favorable electrode composition, and versatile synthesis approach play a significant role in developing advanced electrodes for high-performance supercapacitor. In this work, we report a facile approach for fabricating 1D hierarchical  $\text{CuO@Co}_x\text{Ni}_{1-x}(\text{OH})_2$  nanowire arrays grown on 3D highly conductive copper foam. The optimized  $\text{CuO@Co}_{0.2}\text{Ni}_{0.8}(\text{OH})_2$  electrode delivers an ultrahigh specific capacity of  $374.7 \text{ mAh g}^{-1}$  at  $2 \text{ A g}^{-1}$  with exceptional rate capability ( $301.7 \text{ mAh g}^{-1}$  at  $50 \text{ A g}^{-1}$ ) and remarkable cycling stability (95.9% after 10 000 cycles at  $50 \text{ A g}^{-1}$ ). A flexible asymmetric solid-state supercapacitor (ASC) is fabricated using the optimized  $\text{CuO@Co}_{0.2}\text{Ni}_{0.8}(\text{OH})_2$  as the positive electrode, activated carbon-coated nickel foam as the negative electrode, and polyvinyl alcohol/KOH gel as electrolyte. The flexible ASC operating with a potential window of 0–1.6 V delivers an energy density of  $46.5 \text{ Wh kg}^{-1}$  with a power density of  $526.9 \text{ W kg}^{-1}$ . The ASC also exhibits excellent cycling stability with a capacity retention of 84.3% after 10 000 cycles at a current density of  $7 \text{ A g}^{-1}$ .

**Keywords:** Copper oxide; Nickel–cobalt hydroxide; Copper foam; Nanowire arrays; Flexible asymmetric supercapacitor.

## 1. Introduction

The stringent requirements for reliable supercapacitors have increased because of their rapidly growing commercial markets for electronic devices and electric vehicles [1]. Supercapacitors can be divided into two types based on their charge storage mechanism: electrical double layer capacitors (EDLCs) and pseudocapacitors [2]. EDLCs typically use carbon-based electrodes such as activated carbon, carbon nanotube (CNT), and graphene to accumulate charges at electrode/electrolyte interface [3]. Pseudocapacitors store energy in rapid redox reactions, intercalation, or adsorption process [4]. One of the key challenges for fabricating reliable supercapacitors is manufacturing electrodes with high electrochemical performance. Carbon-based EDLCs provide ultrahigh power density and long cycle life; however, the obtained specific capacity and energy density are relatively low [5]. Specifically, it is impractical to have a pure EDLC based on carbon-based materials since carbon samples are usually composed of defects, dangling atoms and bonds, functionalized groups, dopants, *etc.* [6]. In this context, pseudocapacitive materials have been widely explored as supercapacitor electrode materials.

Co–Ni hydroxides are the most promising candidates because of their ultrahigh theoretical specific capacity [7-9]. Nonetheless, Co–Ni-based hydroxides suffer from low rate capability and limited cycling performance. For example, Liu et al. utilized coprecipitation to synthesize Co–Ni hydroxides/graphene composites, which exhibit a remarkable capability at  $0.5 \text{ A g}^{-1}$  but poor cycling performance ( $\sim 25\%$  decay after 5000 cycles at  $20 \text{ A g}^{-1}$ ) [10]. Huang et al. fabricated Ni–Co@Ni–Co layered double hydroxide (LDH) core/shell nanotube array on carbon fiber cloth. The as-prepared electrode shows

superior capacity at a current density of  $1 \text{ A g}^{-1}$ ; however, the capacity remains 20% of the original value when the current density was increased from 1 to  $20 \text{ A g}^{-1}$ , and only 5000 cycles were tested for cycling stability [11]. Chen et al. developed Ni-Co LDH nanosheet/nickel foam electrode possesses a super-high specific capacity but suffers from a low rate capability (capacity retention  $\sim 63.6\%$  when the current density was increased to  $20 \text{ A g}^{-1}$ ) [7]. The unsatisfactory rate capability/cycling stability could be attributed to the low electrical conductivity, poor ion transport, and large volume expansion at high rates [12]. Accordingly, tremendous efforts have been devoted to resolve these challenges of Ni-Co hydroxides for high-performance supercapacitors. Liu et al. reported the optimal Ni/Co composition ratio to increase the electrochemical surface active sites and the enhancement in the electroactive sites can be ascribed to the possible valence interchange or charge hopping between Co and Ni cations [13]. Gupta et al. reported the direct growth of  $\text{Co}_x\text{Ni}_{1-x}$  LDHs on stainless steel, which led to rapid electron transportation and robust adherence between the active materials and the current collector [14]. Meanwhile, the development of novel current collectors is highly desired. Jiang et al. pioneered the growth of CuO nanowire arrays direct on Cu substrate by an eco-friendly single thermal annealing process [15]. The obtained CuO nanowires were further demonstrated to possess desirable electrical conductivity [16]. However, it is still challenging to combine the aforementioned strategies together.

Inspired by these considerations, herein, we report a two-step facile approach for the synthesis of robust 1D hierarchical  $\text{CuO}@ \text{Co}_x\text{Ni}_{1-x}(\text{OH})_2$  core/shell nanowire arrays directly grown on 3D conductive copper foam (CF) via oxidation followed by electrodeposition. First, CuO nanowire arrays were in situ grown on CF by a facile

oxidation reaction. The nanowire arrays were chosen as the 1D support for the prominent electroactive  $\text{Co}_x\text{Ni}_{1-x}(\text{OH})_2$  nanosheets because of their ease of fabrication via oxidation reaction from CF [17, 18]. Second, ultrathin  $\text{Co}_x\text{Ni}_{1-x}(\text{OH})_2$  nanosheets were electrodeposited on the CuO nanowire arrays to form a hierarchical 1D core/shell nanostructure through the fast and well-controllable electrodeposition method [19]. The proposed electrode architectures offers the advantages of fast electron transport of 1D CuO nanowire arrays, high redox active surface areas of  $\text{Co}_x\text{Ni}_{1-x}(\text{OH})_2$  nanosheets for electrochemical reaction, and robust oxidation-grown CuO nanowire arrays supported for  $\text{Co}_x\text{Ni}_{1-x}(\text{OH})_2$  nanosheets. The molar ratio of Ni/Co in the  $\text{Co}_x\text{Ni}_{1-x}(\text{OH})_2$  nanosheets during electrodeposition was optimized to achieve high electrochemical performance. The optimized  $\text{CuO}@_{\text{Co}_{0.2}\text{Ni}_{0.8}}(\text{OH})_2$  composite shows remarkable electrochemical performance, including ultrahigh specific capacity ( $374.7 \text{ mAh g}^{-1}$  at a current density of  $2 \text{ A g}^{-1}$ ), excellent rate capability (capacity retention of 80.5% on increasing current density from  $2 \text{ A g}^{-1}$  to  $50 \text{ A g}^{-1}$ ), and outstanding cycling stability at high current density (retention of 95.9% over 10 000 cycles at a high density of  $50 \text{ A g}^{-1}$ ). A flexible asymmetric solid-state supercapacitor (ASC) was fabricated using  $\text{CuO}@_{\text{Co}_{0.2}\text{Ni}_{0.8}}(\text{OH})_2$  as the positive electrode, activated carbon (AC) as negative electrode, and polyvinyl alcohol (PVA)/KOH gel as the solid electrolyte. The flexible solid-state ASC operating at a cell voltage of 1.6 V within a potential window of 0–1.6 V delivers an energy density of  $46.5 \text{ Wh kg}^{-1}$  and power density of  $526.9 \text{ W kg}^{-1}$ . The ASC also exhibits excellent cycling stability with capacity retention of 84.3% after 10 000 cycles at a current density of  $7 \text{ A g}^{-1}$ . Results demonstrate that binder-free 1D hierarchical core/shell nanostructures

grown directly on a mesoporous conductive current electrode are promising materials for high-performance supercapacitors.

## 2. Experimental Section

### 2.1 Synthesis of CuO nanowires array

All chemical reagents were of analytical grade and used without further purification. An array of vertically aligned CuO nanowires was fabricated on top of a CF (110 PPI, 1.5 mm thickness,  $0.85 \text{ g cm}^{-3}$ , Artenano Company Limited, Hong Kong) by in situ oxidation. The CF was sequentially cleaned in an ultrasonic bath with acetone, hydrochloric acid (1.5 M), absolute ethanol, and deionized (DI) water. The CF was dried in a vacuum oven and placed in an alumina crucible. The crucible was placed in a muffle furnace and rapidly heated to  $420 \text{ }^\circ\text{C}$  at a heating rate of  $50 \text{ }^\circ\text{C min}^{-1}$  for 4 h.

### 2.2 Synthesis of $\text{CuO}@Co_x\text{Ni}_{1-x}(\text{OH})_2$ composite

CuO nanowires in situ grown on the CF were used as a scaffold for  $\text{Co}_x\text{Ni}_{1-x}(\text{OH})_2$  ultrathin nanosheet shell growth through a facile cathodic electrodeposition method. The electrodeposition was carried out in an electrochemical cell with a three-electrode configuration at room temperature (RT). The CuO nanowire array electrode ( $1 \text{ cm} \times 1 \text{ cm}$ ) was used as the working electrode, a Pt wire as the counter electrode, and the Hg/HgO electrode as reference electrode. The electrolyte for the electrodeposition of  $\text{Co}_x\text{Ni}_{1-x}(\text{OH})_2$  was 50 mL of the metal ion solution containing different  $\text{Co}^{2+}/\text{Ni}^{2+}$  molar ratios of 3:1, 2:1, 2:3, 1:4, and 1:7. The deposition was performed at a potential of  $-1.0 \text{ V}$ , and the synthesis duration was 0–200 s. The samples were removed, rinsed with DI water and absolute ethanol several times, and dried in a vacuum oven. The active materials on

the 3D CF were determined from the mass difference between the CF-supported  $\text{CuO@Co}_x\text{Ni}_{1-x}(\text{OH})_2$  and pure CF substrate. The mass was determined using a semi-micro balance with a readability of 0.1 mg. The area density for  $\text{CuO@Co}_x\text{Ni}_{1-x}(\text{OH})_2$  was  $2 \text{ mg cm}^{-2}$ . For comparison, CF-supported  $\text{CuO@Co}(\text{OH})_2$ ,  $\text{CuO@Ni}(\text{OH})_2$ , and CF-supported  $\text{Co}_x\text{Ni}_{1-x}(\text{OH})_2$  ( $\text{CF@Co}_x\text{Ni}_{1-x}(\text{OH})_2$ ) were also prepared.

### 2.3 Materials characterizations

X-ray diffraction (XRD) patterns were recorded using a SmartLab HR X-ray diffractometer (Cu- $\alpha$  radiation,  $\lambda = 1.5418 \text{ \AA}$ , 40 kV, and 40 mA). Scanning electron microscopy (SEM) investigations were performed on a Nova Nano SEM 450&LEO-155 operated at an acceleration voltage of 15 kV. Transmission electron microscopy (TEM) studies, high-angle annular dark-field scanning TEM-EDS (HAADF-STEM-EDS), and elemental mapping were conducted with an FEI Talos microscope operating at 200 kV accelerating voltage. X-ray photoelectron spectroscopy (XPS) analysis was conducted on a Thermo VG Escalab 250 photoelectron spectrometer.

### 2.4 Electrochemical measurements

The electrochemical performance of the as-obtained  $\text{CuO@Co}_x\text{Ni}_{1-x}(\text{OH})_2$  hybrid electrode ( $1 \text{ cm} \times 1 \text{ cm}$ ) was evaluated using a three-electrode cell configuration on an electrochemical station (ZIVE SP2) at RT in 6 M KOH. A Pt plate and a Hg/HgO electrode were used as counter and reference electrodes, respectively. Cyclic voltammetry (CV) test was performed from 0 V to 0.6 V at various scan rates. Galvanic charging-discharging (GCD) measurements were conducted at current densities from  $2 \text{ A g}^{-1}$  to  $50 \text{ A g}^{-1}$ . Electrochemical impedance spectroscopy (EIS) analysis was performed

within  $10^{-2}$  to  $10^5$  Hz at the open circuit potential with an oscillation amplitude of 5 mV. Cyclic stability was evaluated by GCD measurement at a current density of  $50 \text{ A g}^{-1}$  for 10 000 cycles. The capacity retention of any cycle was obtained through its discharge time divided by the discharge time of the first cycle. The specific capacity derived from the GCD tests was calculated using  $C_s = I \Delta t / (m \Delta V)$ , where  $I$  (A) is the discharge current,  $\Delta t$  is the discharge time,  $m$  (g) is the total weight of the  $\text{CuO@Co}_x\text{Ni}_{1-x}(\text{OH})_2$  composite, and  $\Delta V$  is the potential drop during discharge.

## 2.5 Flexible ASCs

Flexible ASCs were fabricated using  $\text{CuO@Co}_x\text{Ni}_{1-x}(\text{OH})_2$  hybrid as the positive electrode, AC (TFB520) as negative electrode, and PVA/KOH film as electrolyte. An AC electrode was prepared by mixing 95 wt% AC and 5 wt% polytetrafluoroethylene and smearing onto nickel foam (110 PPI, 1.5 mm thickness,  $0.45 \text{ g cm}^{-3}$ , Artenano Company Limited, Hong Kong). The test condition for the electrochemical properties of the individual AC electrode was the same as that of the  $\text{CuO@Co}_x\text{Ni}_{1-x}(\text{OH})_2$  hybrid electrode. Solid PVA/KOH gel electrolyte was prepared as follows: 3 g of PVA (molecular weight: 90 000) and 3 g of KOH were dissolved in 30 mL of DI water under vigorous stirring at  $90^\circ \text{C}$  until the solution became clear. The solution was stirred for another 2 h at RT to eliminate bubbles generated during the dissolution. The solution was then poured into watch glasses to obtain  $\sim 0.1$  mm-thick PVA/KOH gel film. The  $\text{CuO@Co}_x\text{Ni}_{1-x}(\text{OH})_2//\text{AC}$  flexible ASC was fabricated by assembling a PVA/KOH gel film between  $\text{CuO@Co}_x\text{Ni}_{1-x}(\text{OH})_2$  electrode and AC electrode. The as-fabricated device was sealed with parafilm to maintain the stable performance of the SC. ASCs were assembled by two electrodes with different charge storage properties to maintain the

charge balance of the electrodes. The charge balance between the two electrodes follows the relationship of  $q^+ = q^-$ , and  $q$  is calculated in accordance with the equation  $q = C_s \times \Delta V \times m$ . The mass ratio between  $\text{CuO}@Co_xNi_{1-x}(\text{OH})_2$  ( $m_+$ ) electrode and AC ( $m_-$ ) electrode was obtained using the equation  $\frac{m_+}{m_-} = \frac{C_- \Delta V_-}{C_+ \Delta V_+}$ ; thus, the mass ratio of AC to  $\text{CuO}@Co_xNi_{1-x}(\text{OH})_2$  is 7.3. The electrochemical performance of the devices was evaluated on the same electrochemical workstation. Energy ( $E$ , Wh  $\text{kg}^{-1}$ ) and power ( $P$ , W  $\text{kg}^{-1}$ ) density were defined as  $E = \frac{1}{2} \frac{1000 C_s \Delta V^2}{3600}$  and  $P = \frac{3600 E}{\Delta t}$ .

### 3. Results and discussion

We propose a fabrication strategy for  $\text{CuO}@Co_xNi_{1-x}(\text{OH})_2$  core/shell nanowire arrays on CF (Scheme 1). Vapor–liquid–solid mechanism can be used to account for the growth of CuO nanowires [20]. When CF is oxidized in air,  $\text{Cu}_2\text{O}$  film forms on the CF surface.  $\text{Cu}_2\text{O}$  then serves as the seed for CuO growth [15]. The reaction processes involved in the synthesis can be summarized as



CuO nanowires grow through the grain-boundary diffusion of Cu ions across the  $\text{Cu}_2\text{O}$  layer [16]. The slow rate of CuO formation ensures continuous growth mode and uniform diameter for the nanowires.  $\text{Co}_x\text{Ni}_{1-x}(\text{OH})_2$  ultrathin nanosheets are electrodeposited uniformly on the CuO nanowire by electrodeposition to obtain 1D hierarchical arrays of  $\text{CuO}@Co_xNi_{1-x}(\text{OH})_2$  core/shell nanowires supported on CF. The reactions at the deposition potential mainly involve the reduction of nitrate ions ( $\text{NO}_3^-$ ), the interaction

between the cations and  $\text{OH}^-$  generated, and the deposition of double hydroxides on the substrate. During the initial electrodeposition,  $\text{NO}_3^-$  ions are reduced ( $E^0 = -200\text{mV}$ ) on the cathodic surface to produce hydroxide ions (Eq. 3) [21].  $\text{Ni}^{2+}$  and  $\text{Co}^{2+}$  ions and electro-generated  $\text{OH}^-$  form hydroxide deposits and are immobilized on the substrate to offer nucleation sites for hydroxide growth [22]. The electrodeposition process can be expressed as follows:

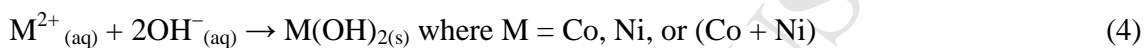


Fig. 1a and S1 show the top-view SEM of CuO on CF. The fluffy surface of CF indicates that its entire surface is covered by CuO nanowires. The nanowires possess smooth surfaces and are uniformly distributed and separated from one another (Fig. 1b). The interspaces between neighboring CuO nanowires can provide sufficient solution contact, leading to homogeneous  $\text{Co}_{0.2}\text{Ni}_{0.8}(\text{OH})_2$  modification. Fig. 1c shows the low-magnification TEM image of a CuO nanowire; such image is consistent with the SEM observations. The high-resolution TEM (HRTEM) image is presented in Fig. 1d. Lattice fringe corresponding to the interplanar distance of 0.23 nm can be indexed to the (200) plane of monoclinic CuO phase. XRD measurements were conducted to determine the phase structure of the final products. The backbone material, namely, CuO nanowires on CF (CF@CuO,  $\text{Cu}_2\text{O}$ : JCPDS card No. 05-0667; CuO: JCPDS card No. 48-1548), was identified based on the XRD pattern in Fig. 1e (blue line). The CuO@ $\text{Co}_{0.2}\text{Ni}_{0.8}(\text{OH})_2$  scratched from the substrate was identified in Fig. 1e (red line). The peaks appearing at  $2\theta$  values of  $11.3^\circ$  ( $7.91 \text{ \AA}$ ),  $22.2^\circ$  ( $4.1 \text{ \AA}$ ),  $34.1^\circ$  ( $2.62 \text{ \AA}$ ), and  $60.5^\circ$  ( $1.52 \text{ \AA}$ ) could be due

to the reflections of the planes (001), (100), (101), and (110), respectively, which correspond to  $\alpha$ -Co(OH)<sub>2</sub> and  $\alpha$ -Ni(OH)<sub>2</sub> [23, 24]. Differentiating between  $\alpha$ -Co(OH)<sub>2</sub> and  $\alpha$ -Ni(OH)<sub>2</sub> phases is difficult because of their similar structures and very close diffraction peaks [25].  $\alpha$ -Co(OH)<sub>2</sub> and  $\alpha$ -Ni(OH)<sub>2</sub> layers are randomly oriented and have a wide interlayer spacing because the interlamellar space contains water molecules bound to the hydroxyl groups by hydrogen bonds; these layers could exhibit superior electrochemical activity [26]. Raman measurements were then conducted on the samples to further explore the properties of the hierarchical hybrid structures (Fig. 1f). The Raman spectrum of CF@CuO shows three peaks at 293.3, 341, and 630.5 cm<sup>-1</sup>, corresponding to the  $A_g$ ,  $B_g^{(1)}$ , and  $B_g^{(2)}$  modes, respectively, of the CuO backbone [27]. The band at 530 cm<sup>-1</sup> in CuO@Co<sub>0.2</sub>Ni<sub>0.8</sub>(OH)<sub>2</sub> was not found in CuO; this band can be assigned to the stretching of M–O (M = Co or Ni) bond in  $\alpha$ -Co(OH)<sub>2</sub> and/or  $\alpha$ -Ni(OH)<sub>2</sub> [28, 29]. After electrochemical deposition, the 3D array of CuO@Co<sub>0.2</sub>Ni<sub>0.8</sub>(OH)<sub>2</sub> nanowires was obtained (Fig. 1g). Each CuO nanowire is fully and uniformly covered by the Co<sub>0.2</sub>Ni<sub>0.8</sub>(OH)<sub>2</sub> nanosheets. The as-obtained array maintains a highly uniform orientation vertical to the substrate. The unique alignment of nanostructures provides a wide electrochemically active surface and short pathways for rapid ion diffusion and electron transport to improve the electrochemical performance [30]. The high-magnification SEM image (Fig. 1h) reveals that the Co<sub>0.2</sub>Ni<sub>0.8</sub>(OH)<sub>2</sub> layer is constructed by perpendicularly cross-linked nanosheets, forming a highly porous surface morphology, which plays a vital role in electrolyte penetration [31]. When viewed at higher magnifications, the nanosheets present a smooth surface and a uniform thickness of ~7 nm (Fig. 1i). The

energy-dispersive X-ray spectroscopy (EDS) map (Fig. S2) demonstrates the homogenous distribution of elements (Ni, Co, Cu, and O).

TEM characterization was performed to elucidate the detailed nanostructure and the phase of the  $\text{CuO@Co}_{0.2}\text{Ni}_{0.8}(\text{OH})_2$  core/shell nanowires. Fig. 2a shows the low-magnification TEM image of an isolated nanowire; in the image, the CuO nanowire core and  $\text{Co}_{0.2}\text{Ni}_{0.8}(\text{OH})_2$  shell ( $\approx 130$  nm) can be clearly distinguished. The gauze-like  $\text{Co}_{0.2}\text{Ni}_{0.8}(\text{OH})_2$  nanosheets were densely grafted along the CuO nanowire uniformly, forming a robust bond to the nanowire. The core/shell feature was verified through cross-sectional analyses by TEM. Fig. 2b shows a typical TEM image of the cross-section of the  $\text{CuO@Co}_{0.2}\text{Ni}_{0.8}(\text{OH})_2$  nanowire. Notably,  $\text{Co}_{0.2}\text{Ni}_{0.8}(\text{OH})_2$  nanosheets are not parallel but vertically grown on the CuO nanowire surface. This result is consistent with the above-mentioned analyses. Fig. 2c displays the HRTEM images of the core/shell nanowire. The visible lattice fringes corresponding to the interplanar distance of 0.25 nm can be attributed to the (1, 1, -1) plane of the CuO phase, and the interplanar distance of 0.234 nm matches well with the (101) planes of  $\text{Co}_{0.2}\text{Ni}_{0.8}(\text{OH})_2$ . In addition, the lattice distortion for both CuO and  $\text{Co}_{0.2}\text{Ni}_{0.8}(\text{OH})_2$  in the interface region suggests the strong interaction between the core and shell [32]. Elemental mapping analyses were performed by HAADF-STEM-EDS to confirm the structure of the  $\text{CuO@Co}_{0.2}\text{Ni}_{0.8}(\text{OH})_2$  nanowire (Fig. 2d). Cu is located in the central part, and Co and Ni are distributed homogeneously in the shell region. The uniform elemental distribution was further identified through the EDS line scan spectra (Fig. S3).

XPS analysis was conducted to characterize the elemental composition and chemical valence states of  $\text{CuO@Co}_{0.2}\text{Ni}_{0.8}(\text{OH})_2$ , confirming the existence of Cu, Co, Ni, C, and

O in Fig. S4. Fig. 2e, f, and g show the high-resolution XPS spectra of Cu 2p, Co 2p, and Ni 2P, respectively. By using the Gaussian fitting method, the XPS spectra for the Cu 2P show the best fit of the spin-orbit split doublet of Cu 2p<sub>3/2</sub> and Cu 2p<sub>1/2</sub> with a separation of 20 eV (Fig. 2e). The fitting peaks at 933.8 and 953.8 eV are indexed to Cu 2p<sub>3/2</sub> and Cu 2p<sub>1/2</sub>, respectively [33]. As shown in Fig. 2f, the fitting peaks at binding energies of 855.5 and 873.2 eV correspond to Ni 2p<sub>3/2</sub> and Ni 2p<sub>1/2</sub>, respectively, along with two satellite peaks. For the XPS spectra of Co 2p, the two prominent peaks located at 780.7 and 796.5 eV can be attributed to Co2p<sub>3/2</sub> and Co2p<sub>1/2</sub>, respectively, and two satellite peaks are located at 785.3 and 802.1 eV (Fig. 2g). Hence, Cu, Co, and Ni are present in the form of Cu<sup>2+</sup>, Co<sup>2+</sup>, and Ni<sup>2+</sup>, respectively, in the CuO@Co<sub>0.2</sub>Ni<sub>0.8</sub>(OH)<sub>2</sub> composite.

To optimize the electrochemical performance of the 1D hierarchical nanowire electrode, we determined the effect of Co<sup>2+</sup>/Ni<sup>2+</sup> molar ratios on the CV and GCD curves. When the other experimental parameters were unchanged, altering the Co<sup>2+</sup>/Ni<sup>2+</sup> molar ratios can tune the electrochemical performance of Co<sub>x</sub>Ni<sub>1-x</sub>(OH)<sub>2</sub>. Fig. 3a shows the CV curves of Co<sub>x</sub>Ni<sub>1-x</sub>(OH)<sub>2</sub>, Co(OH)<sub>2</sub>, and Ni(OH)<sub>2</sub> electrodes at a scan rate of 10 mV s<sup>-1</sup> within the potential window of 0 V to 0.6 V. Co<sub>x</sub>Ni<sub>1-x</sub>(OH)<sub>2</sub>, Co(OH)<sub>2</sub>, and Ni(OH)<sub>2</sub> electrodes show strong redox peaks, which originated mainly from the Faradaic reactions of the surface oxyation species [34]. In the alkaline electrolyte, the Faradaic reactions of Co(OH)<sub>2</sub> and Ni(OH)<sub>2</sub> were based on the equations [35, 36]:



The redox reactions of  $\text{Co}(\text{OH})_2$  involve two steps. In particular, two pairs of redox peaks can be observed for  $\text{Co}(\text{OH})_2$  and  $\text{Co}_x\text{Ni}_{1-x}(\text{OH})_2$  due to the existence of  $\text{Co}^{2+}$ . Notably, the redox peaks are gradually enhanced, and the anodic peaks shift to higher potential with increasing Ni content in the  $\text{Co}_x\text{Ni}_{1-x}(\text{OH})_2$  host slabs [21]. Furthermore, the integral area is the largest for the  $\text{Co}_{0.2}\text{Ni}_{0.8}(\text{OH})_2$ , suggesting the feasibility of rationally tuning the  $\text{Co}^{2+}/\text{Ni}^{2+}$  molar ratio to optimize the electrochemical performance. Fig. 3b shows the symmetrical GCD curves of the as-prepared electrodes at a galvanic current density of  $2 \text{ A g}^{-1}$ , indicating good reversible redox reactions. And energy efficiencies of the  $\text{Co}(\text{OH})_2$ ,  $\text{Co}_x\text{Ni}_{1-x}(\text{OH})_2$ , and  $\text{Ni}(\text{OH})_2$  electrodes were calculated based on the data in Fig. 3b (Fig. S5) [37]. The gravimetric capacity at a current density of  $1 \text{ A g}^{-1}$  were determined to be 85.0, 106.6, 223.2, 350.6, 374.7, 294.1, and 238.9  $\text{mAh g}^{-1}$  for  $\text{CuO@Co}(\text{OH})_2$ ,  $\text{CuO@Co}_{0.75}\text{Ni}_{0.25}(\text{OH})_2$ ,  $\text{CuO@Co}_{0.67}\text{Ni}_{0.33}(\text{OH})_2$ ,  $\text{CuO@Co}_{0.4}\text{Ni}_{0.6}(\text{OH})_2$ ,  $\text{CuO@Co}_{0.2}\text{Ni}_{0.8}(\text{OH})_2$ ,  $\text{CuO@Co}_{0.13}\text{Ni}_{0.87}(\text{OH})_2$ , and  $\text{CuO@Ni}(\text{OH})_2$  (Fig. 3c). Consistent with the CV profiles, the  $\text{Co}_{0.2}\text{Ni}_{0.8}(\text{OH})_2$  electrode exhibits the highest capacity, which is more than 4.4 times higher than that of  $\text{Co}(\text{OH})_2$  and 1.5 times than that of  $\text{Ni}(\text{OH})_2$ . These results can be attributed to the enhancement of the electro-active sites participating in the Faradaic reactions as a result of possible valence interchange or charge hopping between Co and Ni ions since the electro-active sites in Ni–Co bimetallic hydroxides is tunable through various Ni/Co molar ratio [13, 38]. Therefore, the optimized  $\text{CuO@Co}_{0.2}\text{Ni}_{0.8}(\text{OH})_2$  sample was selected to perform electrochemical tests and fabricate flexible ASC.

Fig. 3d shows the CV curves of  $\text{CF@CuO}$  (Fig. S6),  $\text{Co}_{0.2}\text{Ni}_{0.8}(\text{OH})_2$  nanosheets grown on CF ( $\text{CF@Co}_{0.2}\text{Ni}_{0.8}(\text{OH})_2$ ), and  $\text{CuO@Co}_{0.2}\text{Ni}_{0.8}(\text{OH})_2$  electrodes at scan rate of 10

$\text{mV s}^{-1}$  with 6 M KOH as electrolyte. The CV integrated areas of CF@CuO are negligible compared with that of the hybrid electrodes, indicating the negligible contribution of CF@CuO toward the capacity under the conditions adopted in the present work. Moreover, the current density and enclosed CV curve area of the  $\text{CuO@Co}_{0.2}\text{Ni}_{0.8}(\text{OH})_2$  electrode are significantly higher than those of the CF@ $\text{Co}_{0.2}\text{Ni}_{0.8}(\text{OH})_2$  electrode. This finding implies that the  $\text{CuO@Co}_{0.2}\text{Ni}_{0.8}(\text{OH})_2$  electrode possesses high specific capacity and fast redox reaction kinetics because of the synergistic effect of the CuO nanowire arrays and the ultrathin  $\text{Co}_{0.2}\text{Ni}_{0.8}(\text{OH})_2$  nanosheets [39]. The GCD curves of CF@ $\text{Co}_{0.2}\text{Ni}_{0.8}(\text{OH})_2$  and  $\text{CuO@Co}_{0.2}\text{Ni}_{0.8}(\text{OH})_2$  are symmetric and indicate reversible electrochemistry (Fig. S7). Hence, the discharging time for  $\text{CuO@Co}_{0.2}\text{Ni}_{0.8}(\text{OH})_2$  is higher than that for CF@ $\text{Co}_{0.2}\text{Ni}_{0.8}(\text{OH})_2$ .

Fig. 3e presents the CV curves of the typical  $\text{CuO@Co}_{0.2}\text{Ni}_{0.8}(\text{OH})_2$  electrode at various scan rates ranging from  $5 \text{ mV s}^{-1}$  to  $100 \text{ mV s}^{-1}$ . Obvious redox peaks exist in the CV curves, indicating the presence Faradaic reactions between  $\text{CuO@Co}_{0.2}\text{Ni}_{0.8}(\text{OH})_2$  and alkaline electrolytes. With increasing scan rates, the quasi-symmetric redox peaks and similar curve shapes are maintained, implying the prominent reversible redox reaction. The cathodic peak shifts positively, and the anodic peak shifts negatively because of increased ion diffusion resistance [40]. Fig. 3f shows the representative GCD plots of  $\text{CuO@Co}_{0.2}\text{Ni}_{0.8}(\text{OH})_2$  electrode at current densities of 2, 5, 10, 20, 30, 40, and  $50 \text{ A g}^{-1}$ . The GCD curves remain symmetrical even at current densities as high as  $50 \text{ A g}^{-1}$ , indicating superior rate capability. The specific capacity of  $\text{CuO@Co}_{0.2}\text{Ni}_{0.8}(\text{OH})_2$  electrode reaches 374.7, 361.2, 347.1, 328.4, 317.2, 308.1, and  $301.7 \text{ mAh g}^{-1}$ , which correspond to current densities of 2, 5, 10, 20, 30, 40, and  $50 \text{ A g}^{-1}$ , respectively. The

results reveal that the optimized  $\text{CuO@Co}_{0.2}\text{Ni}_{0.8}(\text{OH})_2$  electrode can remarkably retain 80.5% of its initial capacity even when the current density was increased by 25 times. Fig. 3g shows the plot of specific capacity versus current density of the  $\text{Co}_{0.2}\text{Ni}_{0.8}(\text{OH})_2$  and  $\text{CF@Co}_{0.2}\text{Ni}_{0.8}(\text{OH})_2$  electrodes. The specific capacity for the  $\text{CuO@Co}_{0.2}\text{Ni}_{0.8}(\text{OH})_2$  electrode increases by 1.5 times compared with that of the  $\text{CF@Co}_{0.2}\text{Ni}_{0.8}(\text{OH})_2$  electrode ( $244.4 \text{ mAh g}^{-1}$ ). The capacity retention for the  $\text{CuO@Co}_{0.2}\text{Ni}_{0.8}(\text{OH})_2$  electrode is higher than that for the  $\text{CF@Co}_{0.2}\text{Ni}_{0.8}(\text{OH})_2$  electrode (68.6%) when the scan rates were increased from  $2 \text{ A g}^{-1}$  to  $50 \text{ A g}^{-1}$ . EIS analysis was carried out to further understand the exceptional performance of the  $\text{CuO@Co}_{0.2}\text{Ni}_{0.8}(\text{OH})_2$  electrode (Fig. 3h). The Nyquist plots consist of three main distinguishable regions: high-frequency semi-circle, mid-frequency Warburg impedance, and low-frequency capacitive behavior (Fig. S8) [41]. The measured impedance data were analyzed by fitting to an equivalent electrical circuit, which is composed of an equivalent series resistance ( $R_s$ , which includes the intrinsic resistance of active materials, ionic resistance electrolyte, and contact resistance at the active material/current collector interface), charge-transfer resistance ( $R_{ct}$ ), Warburg impedance ( $W$ ), and constant-phase element. The fitting values from the equivalent circuit are shown in Table S1. The  $\text{CuO@Co}_{0.2}\text{Ni}_{0.8}(\text{OH})_2$  electrode shows lower equivalent electrical resistance ( $R_s = 0.16 \ \Omega$ ) than that of the  $\text{CF@Co}_{0.2}\text{Ni}_{0.8}(\text{OH})_2$  electrode ( $R_s = 0.29 \ \Omega$ ). Meanwhile,  $\text{CuO@Co}_{0.2}\text{Ni}_{0.8}(\text{OH})_2$  electrode ( $R_{ct} = 0.23 \ \Omega$ ) possess lower charge transfer resistance than that of  $\text{CF@Co}_{0.2}\text{Ni}_{0.8}(\text{OH})_2$  electrode ( $R_{ct} = 0.41 \ \Omega$ ). The Warburg impedance is associated with the electrolyte ion diffusion length and diffusivity in the electrode [41].  $\text{CuO@Co}_{0.2}\text{Ni}_{0.8}(\text{OH})_2$  electrode exhibits higher CPE-T and CPE-P, and lower Ohmic resistance ( $W$ -R) and diffusion time constant ( $W$ -T)

than that of  $\text{CF@Co}_{0.2}\text{Ni}_{0.8}(\text{OH})_2$  electrode, which implies better capacitive nature and improved diffusion rate of electrolyte ions [42]. The EIS analytical results reveal that the  $\text{CuO@Co}_{0.2}\text{Ni}_{0.8}(\text{OH})_2$  possesses favorable charge-transfer kinetics and rapid electron transport.

The charge–discharge cycling test of 10 000 cycles at  $50 \text{ A g}^{-1}$  was conducted to evaluate the stability of the  $\text{CuO@Co}_{0.2}\text{Ni}_{0.8}(\text{OH})_2$  electrode (Fig. 3i). The specific capacity of the  $\text{CuO@Co}_{0.2}\text{Ni}_{0.8}(\text{OH})_2$  electrode was maintained as 95.9% after 10 000 cycles. The outstanding durability was evident in the SEM images after long-term cycling (Fig. S9). The image shows the preserved well-ordered array structure and hierarchical morphology of the  $\text{CuO@Co}_{0.2}\text{Ni}_{0.8}(\text{OH})_2$  electrode.

The superior performance of the  $\text{CuO@Co}_{0.2}\text{Ni}_{0.8}(\text{OH})_2$  electrode originates from the architectural exquisiteness of the electrode materials and their concomitant unique properties (Fig. 4). This finding can be explained by the following points. (1)  $\text{Co}(\text{OH})_2$  and  $\text{Ni}(\text{OH})_2$  possess intrinsically high pseudocapacitive activities, and the binary metal ions of Ni and Co further enhance the capacitive performance because the mixed valence can increase the number of electro-active sites to superimpose the redox reactions. (2) The 1D hierarchical porous core/shell array configuration leads to an enlarged electrochemically active surface area and multi-access diffusion pathways for facile and rapid ion transport. The ultrathin  $\text{Co}_x\text{Ni}_{1-x}(\text{OH})_2$  nanosheet shells are well separated and form a porous layer surrounding the CuO nanowire core, resulting in full access to the electrolyte. The porous and ultrathin morphologies are essential to alleviate volume change under repeated charge–discharge cycles. (3) The CuO nanowire core grown on a conductive substrate offers a direct electrical pathway from active species to the current

collector. The interfaces of the core/shell are chemically self-assembled and ensure efficient charge transport and good structural integrity. The CuO nanowire core was in situ grown on CF to ensure fast electron transport and excellent structural integrity. (4) Well-aligned CuO@Co<sub>x</sub>Ni<sub>1-x</sub>(OH)<sub>2</sub> nanowire arrays were grown homogeneously on the surface of mesoporous CF current collector to effectively avoid the “dead volume.” All the components, i.e., shell, core, and current collector, build a robust one-body structure, which can effectively tolerate any possible structural deformation and accommodate any mechanical stress, thereby ensuring remarkable flexibility and cyclability.

A flexible ASC device was assembled by employing the CuO@Co<sub>0.2</sub>Ni<sub>0.8</sub>(OH)<sub>2</sub> as the positive electrode, commercially available AC pasted on nickel foam as negative electrode (CV and GCD for AC in Fig. S10, Supplementary Materials), and PVA/KOH as solid electrolyte to demonstrate the practical applicability of the well-designed CuO@Co<sub>0.2</sub>Ni<sub>0.8</sub>(OH)<sub>2</sub> electrode for flexible supercapacitor applications (Fig. 5a). Given that the CuO@Co<sub>0.2</sub>Ni<sub>0.8</sub>(OH)<sub>2</sub> electrode and AC electrodes possess stable potential windows of 0 V to 0.6 V and -1 V to 0 V (Fig. 5b), the operating voltage for the assembled ASC could possibly reach 1.6 V. Fig. 5c shows the CV profiles of the CuO@Co<sub>0.2</sub>Ni<sub>0.8</sub>(OH)<sub>2</sub>//AC ASC at a scan rate of 50 mV s<sup>-1</sup> in different potential windows. The shapes of the CV curves obtained within a wide potential window suggest that both Faradaic reaction and electric double layer contribute to charge storage. The ASC device exhibits stable behavior in the operating window of 0–1.6 V. When the voltage window was further extended to 1.8 V, obvious polarization was observed.

Fig. 5d shows the CV curves of the ASC device measured with a voltage window of 0 V to 1.6 V at scan rates from 5 mV s<sup>-1</sup> to 100 mV s<sup>-1</sup>. Unlike the three-electrode

electrochemical performance featuring obvious redox peaks, the device exhibits a quasi-rectangular CV geometry. With the gradual increase in the scan rate from  $5 \text{ mV s}^{-1}$  to  $100 \text{ mV s}^{-1}$ , the CV curve shows the well-maintained shape and excellent fast charge–discharge behavior of the device. The GCD curves of the ASC device at various current densities are illustrated in Fig. 5e. Voltage plateaus were observed in the GCD curves, consistent with the redox peaks in the CV curves. The nearly symmetrical charge–discharge characteristic indicates high Coulombic efficiency and electrochemical reversibility. The specific capacities of the ASC device were calculated from the GCD curves and plotted as a function of current density (Fig. 5f). The device exhibits a high specific capacity of  $58.2 \text{ mAh g}^{-1}$  based on the total mass of the positive and negative electrodes at  $1 \text{ A g}^{-1}$  and a high rate capability with a specific capacity of  $35.6 \text{ mAh g}^{-1}$  at a high current density of  $10 \text{ A g}^{-1}$ .

To demonstrate the potential application of the ASC in flexible electronic devices, we measured the CV curves under various bending states. The obtained CV curves show no significant change and reveal the excellent flexibility and stability of the device (Fig. 5g). Energy and power densities are two important parameters used to evaluate the performance of energy storage devices. The Ragone plots of  $\text{CuO@Co}_{0.2}\text{Ni}_{0.8}(\text{OH})_2$  derived from the GCD curves are shown in Fig. 5h. Energy density as high as  $46.5 \text{ Wh kg}^{-1}$  was obtained at a power density of  $526.9 \text{ W kg}^{-1}$ , and an energy density of  $28.4 \text{ Wh kg}^{-1}$  was maintained at a high power density of  $7876.9 \text{ W kg}^{-1}$ . The  $\text{CuO@Co}_{0.2}\text{Ni}_{0.8}(\text{OH})_2//\text{AC}$  ASC device exhibits superior performance to those of other trans-metal-based ASCs, such as  $\text{NiCo}_2\text{S}_4@\text{polypyrrole}/\text{AC}$  ( $34.62 \text{ Wh kg}^{-1}$  at  $120.19 \text{ W kg}^{-1}$ ) [43],  $\text{NiCo}_2\text{O}_4@\text{CNT}/\text{CNT}/\text{carbon cloth}$  ( $27.6 \text{ Wh kg}^{-1}$  at  $550 \text{ W kg}^{-1}$ ) [44],

MnO<sub>2</sub>@polypyrrole//AC (25.8 Wh kg<sup>-1</sup> at 901.7 W kg<sup>-1</sup>) [45], MnO<sub>2</sub>/polyaniline//AC (40.2 Wh kg<sup>-1</sup> at 340 W kg<sup>-1</sup>) [46], CoNi<sub>2</sub>O<sub>4</sub>@MnO<sub>2</sub>//AC (37.8 Wh kg<sup>-1</sup> at 187.5 W kg<sup>-1</sup>) [47], Ni-Co-S/graphene//carbon (43.3 Wh kg<sup>-1</sup> at 800 W kg<sup>-1</sup>) [48], NiCo<sub>2</sub>S<sub>4</sub>//graphene (38.64 Wh kg<sup>-1</sup> at 1330 W kg<sup>-1</sup>) [49], Ni/MnO<sub>2</sub>//Ni/Fe<sub>2</sub>O<sub>3</sub> (34.1 Wh kg<sup>-1</sup> at 3197.7 W kg<sup>-1</sup>) [50], FeCo<sub>2</sub>S<sub>4</sub>-NiCo<sub>2</sub>S<sub>4</sub>//FeCo<sub>2</sub>S<sub>4</sub>-NiCo<sub>2</sub>S<sub>4</sub> (46 Wh kg<sup>-1</sup> at 1070 W kg<sup>-1</sup>) [51], NiCo<sub>2</sub>S<sub>4</sub>//carbon (35 Wh kg<sup>-1</sup> at 640 W kg<sup>-1</sup>) [52], g-C<sub>3</sub>N<sub>4</sub>@Ni(OH)<sub>2</sub>//graphene (43.1 Wh kg<sup>-1</sup> at 1870 W kg<sup>-1</sup>) [53], and MnCo<sub>2</sub>O<sub>4.5</sub>//AC (40.5 Wh kg<sup>-1</sup> at 376 W kg<sup>-1</sup>) [54]. The GCD measurement was conducted to evaluate the long-term stability of the ASC device at the current density of 7 A g<sup>-1</sup>. The results show that 84.3% of the initial capacity was retained after 10 000 cycles, indicating the excellent stability of the as-fabricated CuO@Co<sub>0.2</sub>Ni<sub>0.8</sub>(OH)<sub>2</sub>//AC ASC device. Remarkably, the Coulombic efficiency of the ASC devices stayed ≈97% during the 10 000 charge-discharge cycling test (Fig. S11). For practical application, a red light-emitting diode (LED, 1.9 V) was lit by two flexible ASCs connected in series (Fig. 5i inset).

#### 4. Conclusions

In conclusion, we designed and fabricated 1D hierarchical CuO@Co<sub>x</sub>Ni<sub>1-x</sub>(OH)<sub>2</sub> core/shell nanowire arrays in situ grown on CF through a facile oxidation process and fast and well-controllable electrodeposition. The resultant CuO@Co<sub>0.2</sub>Ni<sub>0.8</sub>(OH)<sub>2</sub> electrodes exhibit an ultrahigh specific capacity of 374.7 F g<sup>-1</sup> at a current density of 2 A g<sup>-1</sup>, superior rate capability of 80.5% at 50 A g<sup>-1</sup>, and extremely long cycle stability with capacity retention of 95.9% after 10 000 charge-discharge cycles at 50 A g<sup>-1</sup>. The superior performance could be attributed to the excellent electrical conductivity of metallic mesoporous Cu foam, 1D electron transport highway of CuO nanowire arrays,

and outstanding pseudocapacitive properties of the  $\text{Co}_x\text{Ni}_{1-x}(\text{OH})_2$  ultrathin nanosheets with a large surface area and porous morphology. A flexible ASC device was assembled using  $\text{CuO@Co}_{0.2}\text{Ni}_{0.8}(\text{OH})_2$  electrodes as the positive electrode, AC on nickel foam as negative electrode, and PVA/KOH as electrolyte to demonstrate the practical application of the high-performance pseudocapacitive electrodes. The maximum specific energy density of  $46.5 \text{ Wh kg}^{-1}$  and specific power of  $7876.9 \text{ W kg}^{-1}$  were obtained with an operational potential range of 1.6 V. Hence, the rational design of 1D hierarchical core/shell arrays is an effective approach to realize high specific capacity, high rate capability, and long cycle stability for high-performance supercapacitors. Furthermore, this hierarchical nanostructure arrays may be applicable to other energy conversion and storage systems, such as lithium-ion batteries, water splitting devices, and fuel cells.

### **Acknowledgements**

This work is supported by the GDUT Start-up Research Grant (220413252); the Science and Technology Development Fund of the Macau SAR [FDCT-098/2015/A3 and FDCT-191/2017/A3]; the Multi-Year Research Grants from the Research & Development Office at the University of Macau [MYRG2017-00216-FST]; and the UEA funding.

## References

- [1] G.Q. Tan, F. Wu, Y.F. Yuan, R.J. Chen, T. Zhao, Y. Yao, J. Qian, J.R. Liu, Y.S. Ye, R. Shahbazian-Yassar, J. Lu, K. Amine, Freestanding three-dimensional core-shell nanoarrays for lithium-ion battery anodes, *Nat. Commun.*, 7 (2016) 11774.
- [2] S.X. Wu, K.S. Hui, K.N. Hui, 2D Black Phosphorus: from Preparation to applications for electrochemical energy storage, *Adv. Sci.*, 5 (2018) 1700491.
- [3] F.S. Wen, C.X. Hao, J.Y. Xiang, L.M. Wang, H. Hou, Z.B. Su, W.T. Hu, Z.Y. Liu, Enhanced laser scribed flexible graphene-based micro-supercapacitor performance with reduction of carbon nanotubes diameter, *Carbon*, 75 (2014) 236-243.
- [4] S.X. Wu, K. San Hui, K.N. Hui, Carbon nanotube@manganese oxide nanosheet core-shell structure encapsulated within reduced graphene oxide film for flexible all-solid-state asymmetric supercapacitors, *Carbon*, 132 (2018) 776-784.
- [5] P. Simon, Y. Gogotsi, B. Dunn, Where do batteries end and supercapacitors begin?, *Science*, 343 (2014) 1210-1211.
- [6] A. Eftekhari, M. Mohamedi, Tailoring pseudocapacitive materials from a mechanistic perspective, *Mater. Today Energy*, 6 (2017) 211-229.
- [7] S.X. Wu, K.S. Hui, K.N. Hui, One-dimensional core-shell architecture composed of silver nanowire@hierarchical nickel-aluminum layered double hydroxide nanosheet as advanced electrode materials for pseudocapacitor, *J. Phys. Chem. C*, 119 (2015) 23358-23365.
- [8] S.X. Wu, K.S. Hui, K.N. Hui, K.H. Kim, Electrostatic-induced assembly of graphene-encapsulated carbon@nickel-aluminum layered double hydroxide core-shell spheres

hybrid structure for high-energy and high-power-density asymmetric supercapacitor, *ACS Appl. Mater. Interfaces*, 9 (2017) 1395-1406.

[9] S. Wu, K.S. Hui, K.N. Hui, J.M. Yun, K.H. Kim, Silver particle-loaded nickel oxide nanosheet arrays on nickel foam as advanced binder-free electrodes for aqueous asymmetric supercapacitors, *RSC Adv.*, 7 (2017) 41771-41778.

[10] Y.W. Cheng, H.B. Zhang, C.V. Varanasi, J. Liu, Improving the performance of cobalt-nickel hydroxidebased self-supporting electrodes for supercapacitors using accumulative approaches, *Energy Environ. Sci.*, 6 (2013) 3314-3321.

[11] Y. Liu, N. Fu, G. Zhang, M. Xu, W. Lu, L. Zhou, H. Huang, Design of hierarchical Ni Co@ Ni Co layered double hydroxide core-shell structured nanotube array for high-performance flexible all-solid-state battery-type supercapacitors, *Adv. Funct. Mater.*, 27 (2017) 1605307.

[12] G. Nagaraju, S.C. Sekhar, B. Ramulu, L.K. Bharat, G.S.R. Raju, Y.K. Han, J.S. Yu, Enabling redox chemistry with hierarchically designed bilayered nanoarchitectures for pouch-type hybrid supercapacitors: a sunlight-driven rechargeable energy storage system to portable electronics, *Nano Energy*, 50 (2018) 448-461.

[13] X.H. Liu, R.Z. Ma, Y. Bando, T. Sasaki, A general strategy to layered transition-metal hydroxide nanocones: tuning the composition for high electrochemical performance, *Adv. Mater.*, 24 (2012) 2148-2153.

[14] V. Gupta, S. Gupta, N. Miura, Potentiostatically deposited nanostructured  $\text{Co}_x\text{Ni}_{1-x}$  layered double hydroxides as electrode materials for redox-supercapacitors, *J. Power Sources*, 175 (2008) 680-685.

- [15] X.C. Jiang, T. Herricks, Y.N. Xia, CuO nanowires can be synthesized by heating copper substrates in air, *Nano Lett.*, 2 (2002) 1333-1338.
- [16] A.M.B. Goncalves, L.C. Campos, A.S. Ferlauto, R.G. Lacerda, On the growth and electrical characterization of CuO nanowires by thermal oxidation, *J. Appl. Phys.*, 106 (2009) 034303.
- [17] Z. Yu, J. Thomas, Energy storing electrical cables: integrating energy storage and electrical conduction, *Adv. Mater.*, 26 (2014) 4279-4285.
- [18] Z. Yu, J. Moore, J. Calderon, L. Zhai, J. Thomas, Coil-type asymmetric supercapacitor electrical cables, *Small*, 11 (2015) 5289-5295.
- [19] X. Xia, J. Tu, Y. Zhang, J. Chen, X. Wang, C. Gu, C. Guan, J. Luo, H.J. Fan, Porous hydroxide nanosheets on preformed nanowires by electrodeposition: branched nanoarrays for electrochemical energy storage, *Chem. Mater.*, 24 (2012) 3793-3799.
- [20] Y.Y. Wu, P.D. Yang, Direct observation of vapor-liquid-solid nanowire growth, *J. Am. Chem. Soc.*, 123 (2001) 3165-3166.
- [21] S.B. Kulkarni, A.D. Jagadale, V.S. Kumbhar, R.N. Bulakhe, S.S. Joshi, C.D. Lokhande, Potentiodynamic deposition of composition influenced  $\text{Co}_{1-x}\text{Ni}_x$  LDHs thin film electrode for redox supercapacitors, *Int. J. Hydrogen. Energ.*, 38 (2013) 4046-4053.
- [22] Y. Li, L. Zhang, X. Xiang, D.P. Yan, F. Li, Engineering of ZnCo-layered double hydroxide nanowalls toward high-efficiency electrochemical water oxidation, *J. Mater. Chem. A*, 2 (2014) 13250-13258.
- [23] Z.P. Liu, R.Z. Ma, M. Osada, K. Takada, T. Sasaki, Selective and controlled synthesis of alpha- and beta-cobalt hydroxides in highly developed hexagonal platelets, *J. Am. Chem. Soc.*, 127 (2005) 13869-13874.

- [24] V. Gupta, T. Kusahara, H. Toyama, S. Gupta, N. Miura, Potentiostatically deposited nanostructured  $\alpha$ -Co(OH)<sub>2</sub>: A high performance electrode material for redox-capacitors, *Electrochem. Commun.*, 9 (2007) 2315-2319.
- [25] V. Gupta, S. Gupta, N. Miura, Statically deposited nanostructured Co<sub>x</sub>Ni<sub>1-x</sub> layered double hydroxides as electrode materials for redox-supercapacitors, *J. Power Sources*, 175 (2008) 680-685.
- [26] Z.A. Hu, Y.L. Xie, Y.M. Wang, H.Y. Wu, Y.Y. Yang, Z.Y. Zhang, Synthesis and electrochemical characterization of mesoporous Co<sub>x</sub>Ni<sub>1-x</sub> layered double hydroxides as electrode materials for supercapacitors, *Electrochim. Acta*, 54 (2009) 2737-2741.
- [27] X.K. Chen, J.C. Irwin, J.P. Franck, Evidence for a strong spin-phonon interaction in cupric oxide, *Phys. Rev. B*, 52 (1995) 13130-13133.
- [28] W.J. Zhou, X.H. Cao, Z.Y. Zeng, W.H. Shi, Y.Y. Zhu, Q.Y. Yan, H. Liu, J.Y. Wang, H. Zhang, One-step synthesis of Ni<sub>3</sub>S<sub>2</sub> nanorod@Ni(OH)<sub>2</sub> nanosheet core-shell nanostructures on a three-dimensional graphene network for high-performance supercapacitors, *Energy Environ. Sci.*, 6 (2013) 2216-2221.
- [29] J. Yang, H.W. Liu, W.N. Martens, R.L. Frost, Synthesis and characterization of cobalt hydroxide, cobalt oxyhydroxide, and cobalt oxide nanodiscs, *J. Phys. Chem. C*, 114 (2010) 111-119.
- [30] Q.C. Zhang, X.N. Wang, Z.H. Pan, J. Sun, J.X. Zhao, J. Zhang, C.X. Zhang, L. Tang, J. Luo, B. Song, Z.X.X. Zhang, W.B. Lu, Q.W. Li, Y.G. Zhang, Y.G. Yao, Wrapping aligned carbon nanotube composite sheets around vanadium nitride nanowire arrays for asymmetric coaxial fiber-shaped supercapacitors with ultrahigh energy density, *Nano Lett.*, 17 (2017) 2719-2726.

- [31] L.L. Li, S.J. Peng, H.B. Wu, L. Yu, S. Madhavi, X.W. Lou, A flexible quasi-solid-state asymmetric electrochemical capacitor based on hierarchical porous  $V_2O_5$  nanosheets on carbon nanofibers, *Adv. Energy Mater.*, 5 (2015) 1500753.
- [32] K.B. Kim, J. Das, F. Baier, J. Eckert, Lattice distortion/disordering and local amorphization in the dendrites of a  $Ti_{66.1}Cu_8Ni_{4.8}Sn_{7.2}Nb_{13.9}$  nanostructure-dendrite composite during intersection of shear bands, *Appl. Phys. Lett.*, 86 (2005) 171909.
- [33] F. Klein, R. Pinedo, P. Hering, A. Polity, J.r. Janek, P. Adelhelm, Reaction mechanism and surface film formation of conversion materials for lithium-and sodium-ion batteries: an XPS case study on sputtered copper oxide (CuO) thin film model electrodes, *J. Phys. Chem. C*, 120 (2016) 1400-1414.
- [34] L. Huang, D.C. Chen, Y. Ding, S. Feng, Z.L. Wang, M.L. Liu, Nickel-cobalt hydroxide nanosheets coated on  $NiCo_2O_4$  nanowires grown on carbon fiber paper for high-performance pseudocapacitors, *Nano Lett.*, 13 (2013) 3135-3139.
- [35] S.X. Wu, K.S. Hui, K.N. Hui, K.H. Kim, Ultrathin porous NiO nanoflake arrays on nickel foam as an advanced electrode for high performance asymmetric supercapacitors, *J. Mater. Chem. A*, 4 (2016) 9113-9123.
- [36] Y.Y. Liang, S.J. Bao, H.L. Li, Nanocrystalline nickel cobalt hydroxides/ultrastable Y zeolite composite for electrochemical capacitors, *J. Solid State Electr.*, 11 (2007) 571-576.
- [37] A. Eftekhari, Energy efficiency: a critically important but neglected factor in battery research, *Sustainable Energy Fuels*, 1 (2017) 2053-2060.

- [38] P.Y. Yang, Z.Y. Wu, Y.C. Jiang, Z.C. Pan, W.C. Tian, L. Jiang, L.F. Hu, Fractal  $(\text{Ni}_x\text{Co}_{1-x})_9\text{Se}_8$  nanodendrite arrays with highly exposed (011) surface for wearable, all-solid-state supercapacitor, *Adv. Energy Mater.*, 8 (2018) 1801392.
- [39] S. Li, Y. Chang, J. Yang, Z. Changtai, M. Zhang, H. Huang, L. Zhibin, W. Guo, J. Qiu, Superhydrophilic “nanoglue” stabilizing the metal hydroxides onto carbon materials for high-energy and ultralong-life asymmetric supercapacitors, *Energy Environ. Sci.*, 10 (2017) 1958.
- [40] Y.G. Wang, H.Q. Li, Y.Y. Xia, Ordered whiskerlike polyaniline grown on the surface of mesoporous carbon and its electrochemical capacitance performance, *Adv. Mater.*, 18 (2006) 2619-2623.
- [41] A. Eftekhari, The mechanism of ultrafast supercapacitors, *J. Mater. Chem. A*, 6 (2018) 2866-2876.
- [42] S. Kandula, K.R. Shrestha, N.H. Kim, J.H. Lee, Fabrication of a 3D hierarchical sandwich  $\text{Co}_9\text{S}_8/\alpha\text{-MnS}@N\text{-C}@MoS_2$  nanowire architectures as advanced electrode material for high performance hybrid supercapacitors, *Small*, 14 (2018) 1800291.
- [43] M.L. Yan, Y.D. Yao, J.Q. Wen, L. Long, M.L. Kong, G.G. Zhang, X.M. Liao, G.F. Yin, Z.B. Huang, Construction of a hierarchical  $\text{NiCo}_2\text{S}_4@PPy$  core shell Heterostructure nanotube array on Ni foam for a high-performance asymmetric supercapacitor, *ACS Appl. Mater. Interfaces*, 8 (2016) 24525-24535.
- [44] P. Wu, S. Cheng, M. Yao, L. Yang, Y. Zhu, P. Liu, O. Xing, J. Zhou, M. Wang, H. Luo, A low-cost, self-standing  $\text{NiCo}_2\text{O}_4@CNT/CNT$  multilayer electrode for flexible asymmetric solid-state supercapacitors, *Adv. Funct. Mater.*, 27 (2017) 1702160.

- [45] W.D. He, C.G. Wang, F.W. Zhuge, X.L. Deng, X.J. Xu, T.Y. Zhai, Flexible and high energy density asymmetrical supercapacitors based on core/shell conducting polymer nanowires/manganese dioxide nanoflakes, *Nano Energy*, 35 (2017) 242-250.
- [46] N. Liu, Y.L. Su, Z. Wang, Z. Wang, J. Xia, Y. Chen, Z. Zhao, Q. Li, F. Geng, Electrostatic interaction-assisted construction of 3D networks of manganese dioxide nanosheets for flexible high-performance solid-state asymmetric supercapacitors, *ACS nano*, 11 (2017) 7879.
- [47] Y.B. Zhang, B. Wang, F. Liu, J.P. Cheng, X.W. Zhang, L. Zhang, Full synergistic contribution of electrodeposited three-dimensional  $\text{NiCo}_2\text{O}_4@ \text{MnO}_2$  nanosheet networks electrode for asymmetric supercapacitors, *Nano Energy*, 27 (2016) 627-637.
- [48] J. Yang, C. Yu, X.M. Fan, S.X. Liang, S.F. Li, H.W. Huang, Z. Ling, C. Hao, J.S. Qiu, Electroactive edge site-enriched nickel-cobalt sulfide into graphene frameworks for high-performance asymmetric supercapacitors, *Energy Environ. Sci.*, 9 (2016) 1299-1307.
- [49] F. Lu, M. Zhou, W.R. Li, Q.H. Weng, C.L. Li, Y.M. Xue, X.F. Jiang, X.H. Zeng, Y. Bando, D. Golberg, Engineering sulfur vacancies and impurities in  $\text{NiCo}_2\text{S}_4$  nanostructures toward optimal supercapacitive performance, *Nano Energy*, 26 (2016) 313-323.
- [50] Y. Li, J. Xu, T. Feng, Q.F. Yao, J.P. Xie, H. Xia,  $\text{Fe}_2\text{O}_3$  nanoneedles on ultrafine nickel nanotube arrays as efficient anode for high-performance asymmetric supercapacitors, *Adv. Funct. Mater.*, 27 (2017) 1606728.
- [51] J. Zhu, S.C. Tang, J. Wu, X.L. Shi, B.G. Zhu, X.K. Meng, Wearable high-performance supercapacitors based on silver-sputtered textiles with  $\text{FeCo}_2\text{S}_4\text{-NiCo}_2\text{S}_4$

composite nanotube-built multitripod architectures as advanced flexible electrodes, *Adv. Energy Mater.*, 7 (2017) 1601234.

[52] Q. Wang, F. Gao, B. Xu, F. Cai, F. Zhan, F. Gao, Q. Wang, ZIF-67 derived amorphous  $\text{CoNi}_2\text{S}_4$  nanocages with nanosheet arrays on the shell for a high-performance asymmetric supercapacitor, *Chem. Eng. J.*, 327 (2017) 387-396.

[53] B. Dong, M. Li, S. Chen, D. Ding, W. Wei, G. Gao, S. Ding, Formation of  $\text{g-C}_3\text{N}_4@\text{Ni}(\text{OH})_2$  honeycomb nanostructure and asymmetric supercapacitor with high energy and power density, *ACS Appl. Mater. Interfaces*, 9 (2017) 170890.

[54] L. Kuang, F. Ji, X. Pan, D. Wang, X. Chen, D. Jiang, Y. Zhang, B. Ding, Mesoporous  $\text{MnCo}_2\text{O}_{4.5}$  nanoneedle arrays electrode for high-performance asymmetric supercapacitor application, *Chem. Eng. J.*, 315 (2017) 491-499.

### Figure captions

**Scheme 1.** Schematic of the fabrication process. CuO nanowire array was grown in situ onto the CF through thermal oxidation.  $\text{Co}_x\text{Ni}_{1-x}(\text{OH})_2$  ultrathin nanosheets were electrodeposited on CuO nanowire arrays.

**Fig. 1.** (a, b) SEM images of CF@CuO. (c) TEM and (d) HRTEM images of the CuO nanowire. (e) XRD patterns and (f) Raman spectra of CF@CuO and  $\text{CuO}@_{\text{Co}_{0.2}\text{Ni}_{0.8}}(\text{OH})_2$ . (g-i) SEM images of  $\text{CuO}@_{\text{Co}_{0.2}\text{Ni}_{0.8}}(\text{OH})_2$  with different magnifications. Inset in (i) shows the corresponding magnified nanosheet structure.

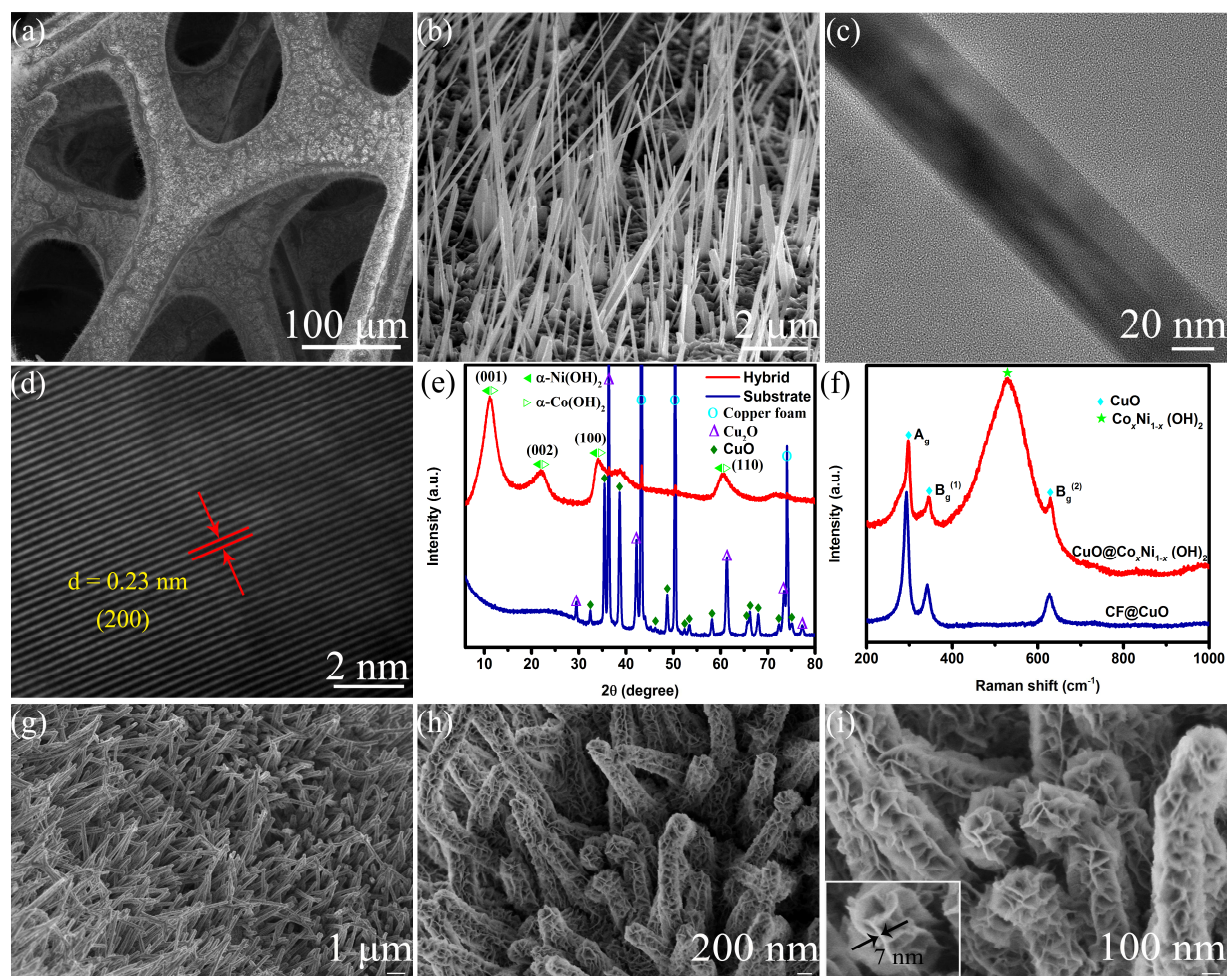
**Fig. 2.** (a) TEM images of  $\text{CuO}@_{\text{Co}_{0.2}\text{Ni}_{0.8}}(\text{OH})_2$  at different magnifications. (b) TEM, (c) HRTEM cross-section of the FIB-cut  $\text{CuO}@_{\text{Co}_{0.2}\text{Ni}_{0.8}}(\text{OH})_2$  nanowire. (d) Corresponding EDS mapping images for Co, Ni, Cu, and O in the  $\text{CuO}@_{\text{Co}_{0.2}\text{Ni}_{0.8}}(\text{OH})_2$  nanowire cross-section. High-resolution XPS spectra of Cu 2p (e), Ni 2p (f), and Co 2p (g) core levels in  $\text{CuO}@_{\text{Co}_{0.2}\text{Ni}_{0.8}}(\text{OH})_2$ .

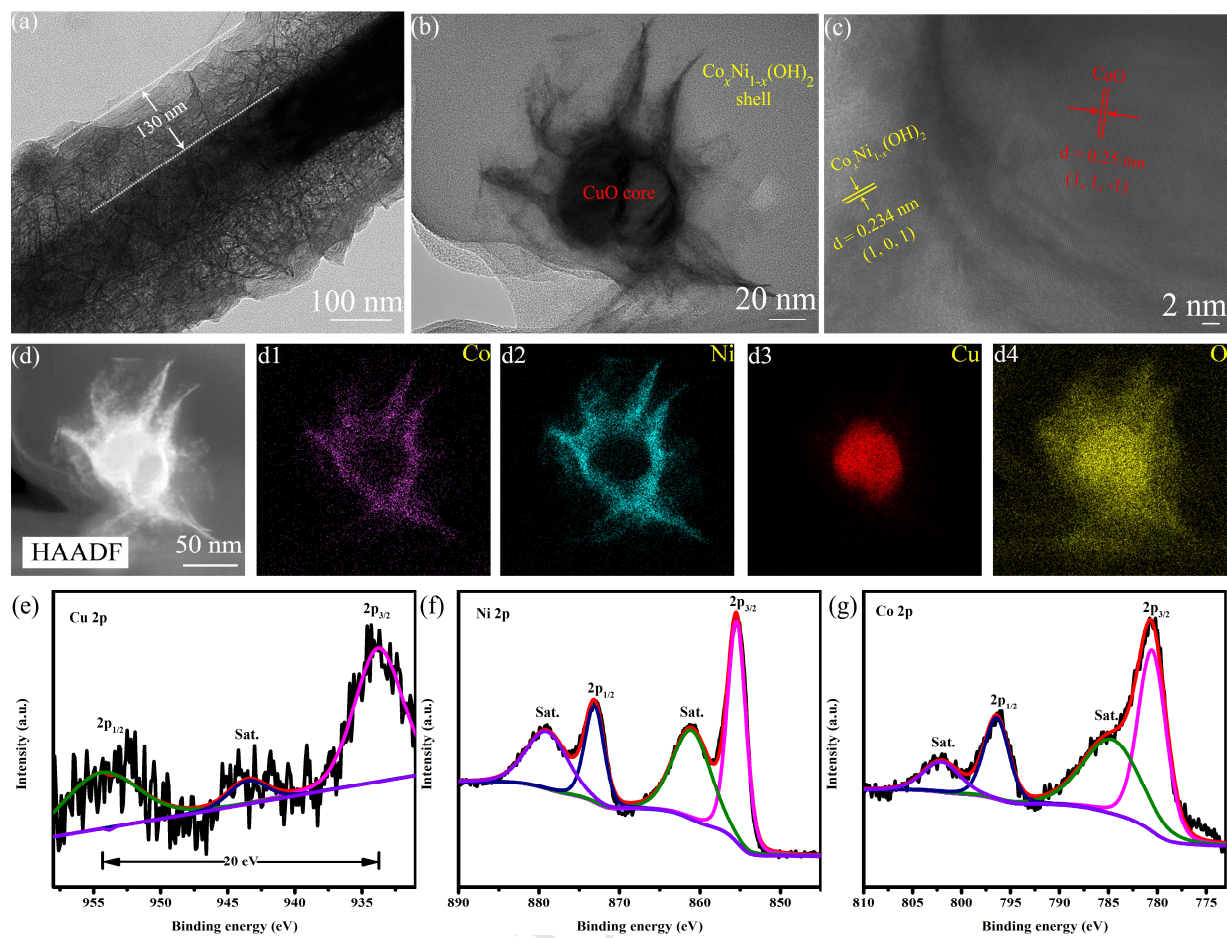
**Fig. 3.** (a) CV curves of  $\text{Co}_x\text{Ni}_{1-x}(\text{OH})_2$ ,  $\text{Co}(\text{OH})_2$ , and  $\text{Ni}(\text{OH})_2$  electrodes at a scan rate of  $10 \text{ mV s}^{-1}$ . (b) GCD curves of  $\text{Co}_x\text{Ni}_{1-x}(\text{OH})_2$ ,  $\text{Co}(\text{OH})_2$ , and  $\text{Ni}(\text{OH})_2$  electrodes at a current density of  $2 \text{ A g}^{-1}$ . (c) Specific capacity of  $\text{Co}_x\text{Ni}_{1-x}(\text{OH})_2$ ,  $\text{Co}(\text{OH})_2$ , and  $\text{Ni}(\text{OH})_2$  electrodes at a current density of  $2 \text{ A g}^{-1}$ . (d) CV curves of CF@CuO, CF@ $\text{Co}_{0.2}\text{Ni}_{0.8}(\text{OH})_2$ , and  $\text{CuO}@_{\text{Co}_{0.2}\text{Ni}_{0.8}}(\text{OH})_2$  electrodes. (e) CV curves of  $\text{CuO}@_{\text{Co}_{0.2}\text{Ni}_{0.8}}(\text{OH})_2$  at different scan rates. (f) GCD curves of  $\text{CuO}@_{\text{Co}_{0.2}\text{Ni}_{0.8}}(\text{OH})_2$  at different current densities. (g) Specific capacity of CF@ $\text{Co}_{0.2}\text{Ni}_{0.8}(\text{OH})_2$  and  $\text{CuO}@_{\text{Co}_{0.2}\text{Ni}_{0.8}}(\text{OH})_2$  electrodes at different current densities. (h) EIS curves of CF@ $\text{Co}_{0.2}\text{Ni}_{0.8}(\text{OH})_2$  and  $\text{CuO}@_{\text{Co}_{0.2}\text{Ni}_{0.8}}(\text{OH})_2$  electrodes. (i) Cycling performance of

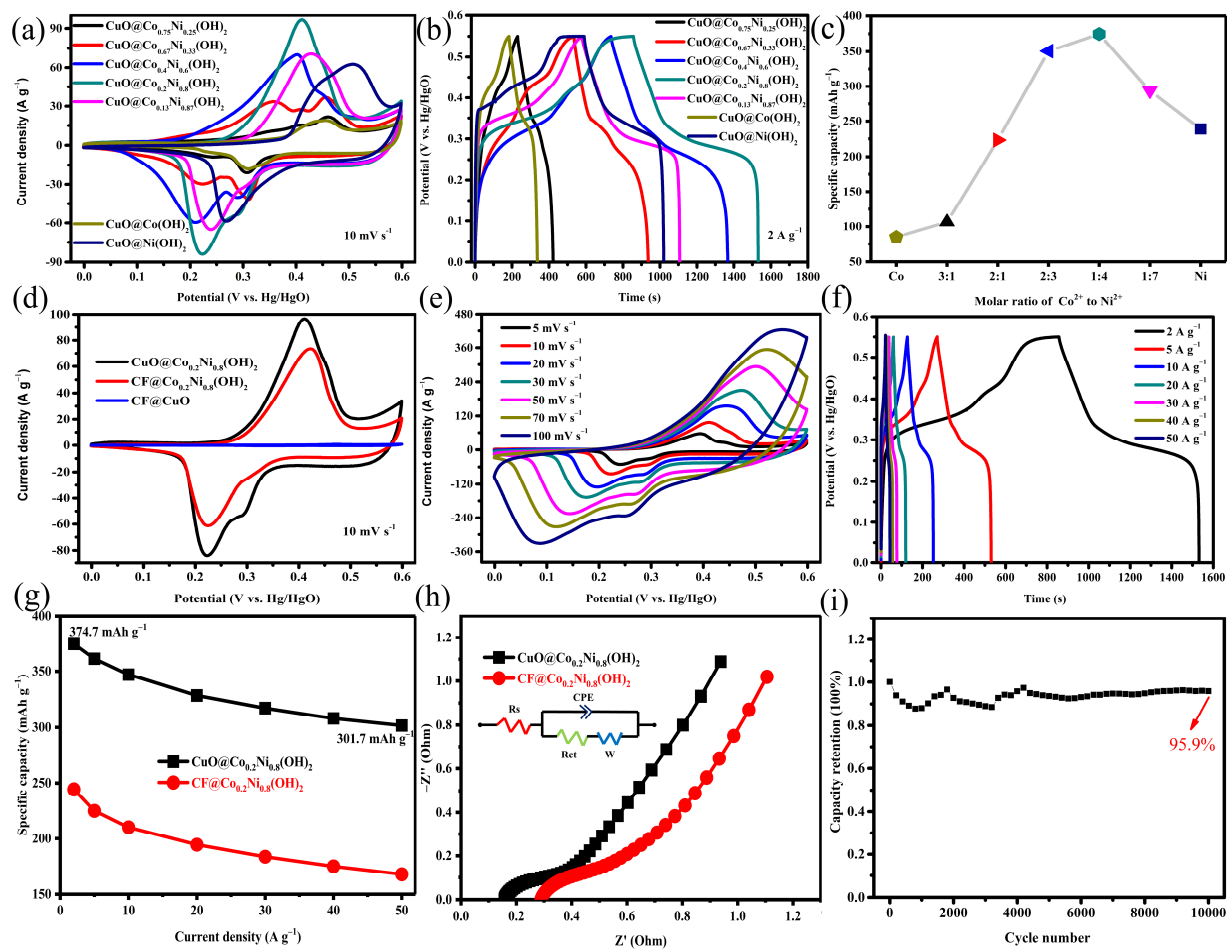
CuO@Co<sub>0.2</sub>Ni<sub>0.8</sub>(OH)<sub>2</sub> electrode at a current density of 50 A g<sup>-1</sup> up to 10 000 cycling charge–discharge tests.

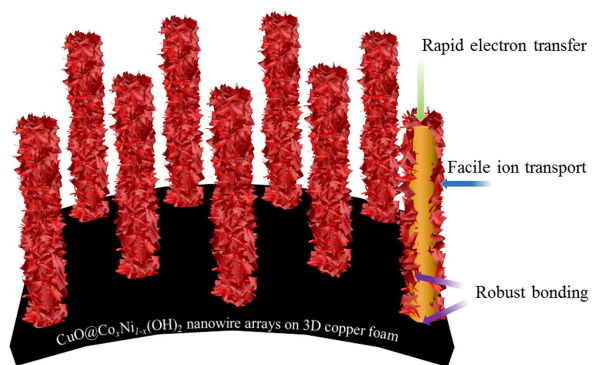
**Fig. 4.** Electrode design of Co<sub>x</sub>Ni<sub>1-x</sub>(OH)<sub>2</sub>. Each component provides different functionalities.

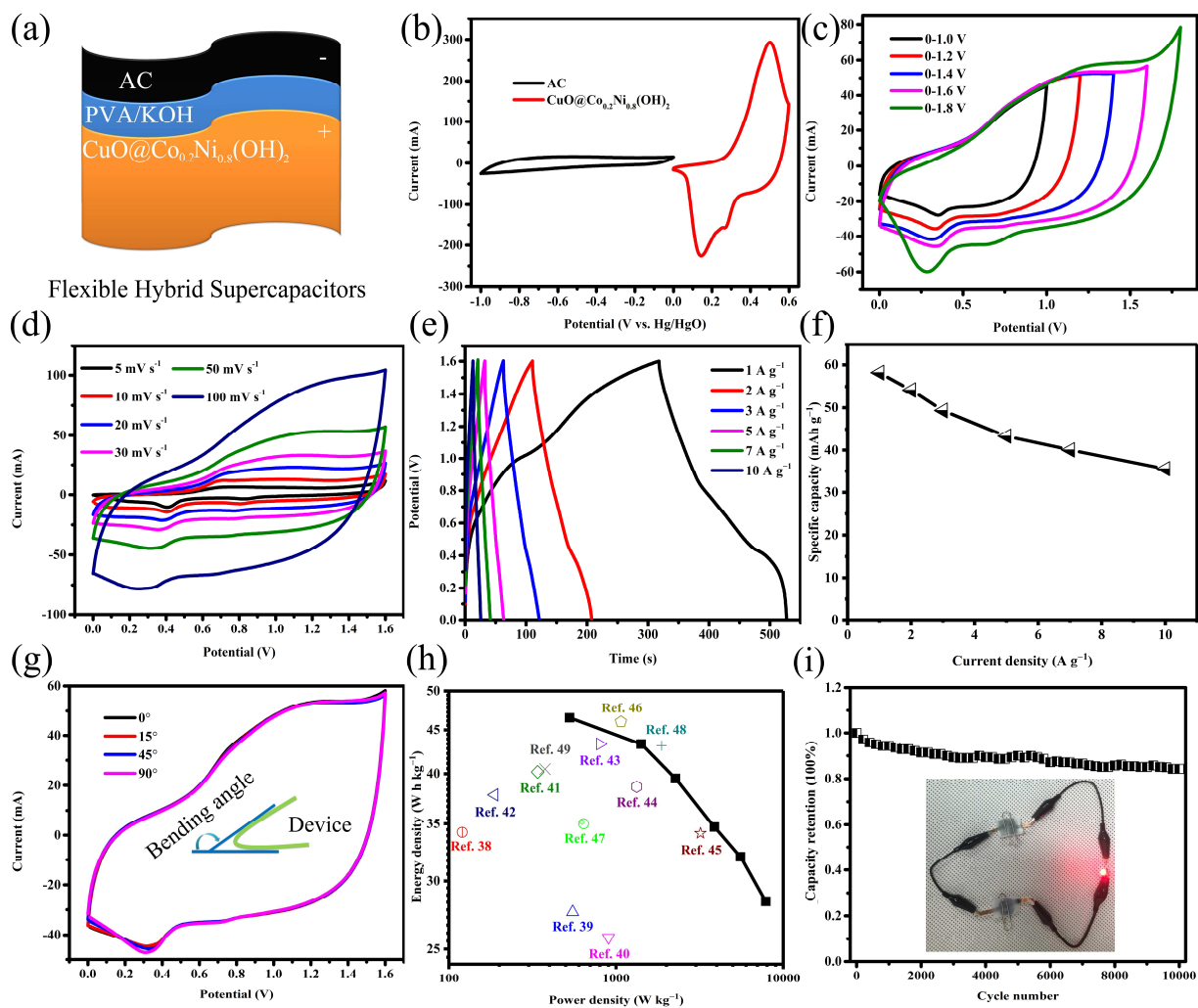
**Fig. 5.** (a) Schematic of the CuO@Co<sub>0.2</sub>Ni<sub>0.8</sub>(OH)<sub>2</sub>//AC flexible ASC configuration. (b) CV curves of the CuO@Co<sub>0.2</sub>Ni<sub>0.8</sub>(OH)<sub>2</sub> electrode and AC electrode in separate potential windows at a scan rate of 50 mV s<sup>-1</sup>. (c) CV curves of the CuO@Co<sub>0.2</sub>Ni<sub>0.8</sub>(OH)<sub>2</sub>//AC in different voltage windows at a scan rate of 50 mV s<sup>-1</sup>. (d) CV curves of the flexible device at different scan rates. (e) GCD curves at various current densities. (f) Specific capacity at different current densities. (g) CV curves of the flexible device under different bending conditions at a scan rate of 50 mV s<sup>-1</sup>. (h) Ragone plot of the CuO@Co<sub>0.2</sub>Ni<sub>0.8</sub>(OH)<sub>2</sub>//AC flexible ASC and previously reported SCs in literature. (i) Cycling performance of the CuO@Co<sub>0.2</sub>Ni<sub>0.8</sub>(OH)<sub>2</sub>//AC flexible ASC at a current density of 7 A g<sup>-1</sup> for 10 000 cycles; inset shows an LED lit by the ASC devices connected in series.

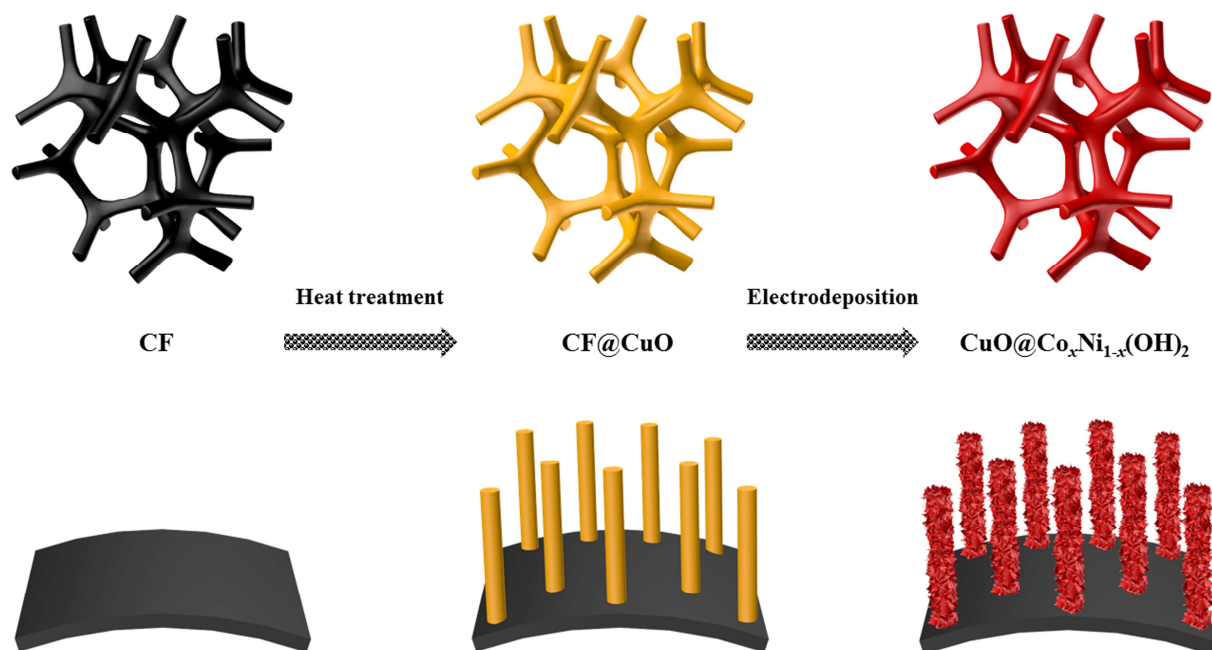












ACCEPTED MANUSCRIPT

**Highlights**

- CuO@Co<sub>x</sub>Ni<sub>1-x</sub>(OH)<sub>2</sub> nanowire arrays grown on 3D copper foam was fabricated.
- The architecture delivered an ultrahigh specific capacity.
- Flexible hybrid supercapacitor using CuO@Co<sub>0.2</sub>Ni<sub>0.8</sub>(OH)<sub>2</sub> was assembled.
- The flexible devices displayed excellent electrochemical performance.